Friction https://mc03.manuscriptcentral.com/friction
https://doi.org/10.26599/FRICT.2026.9441216

Research Article

Mechanistic investigation of friction-induced vibration and noise behaviors of lightweight brake material

Caiqi Liao[1], Jiliang Mo[1, 2], Quan Wang[1], Zhiwei Wang[1, 2], Qixiang Zhang[1, 2*], Wenwei Jin[3]

[1] *School of Mechanical Engineering, Southwest Jiaotong University, Chengdu, Sichuan 610031, China*

[2] *State Key Laboratory of Rail Transit Vehicle System, Southwest Jiaotong University, Chengdu, Sichuan 610031, China*

[3] *CRRC Qishuyan Co., LTD, Changzhou, Jiangsu 213011, China*

* Corresponding author: Qixiang Zhang, E-mail: Zqx137@my.swjtu.edu.cn

Received: September 30, 2025; Revised: December 8, 2025; Accepted: January 7, 2026

© The Author(s) 2026.

Just Accepted

Abstract: The vibration and noise issues of lightweight friction pairs in suburban train braking systems have become a critical bottleneck restricting their engineering application. This study investigated the lightweight friction pairs composed of three representative synthetic brake pads and an aluminum matrix composite brake disc. Utilizing tribological tests, interfacial wear analysis, and dynamic modelling, the study investigated the impact of interfacial wear and contact behaviors on vibration and noise, and elucidated the mechanisms by which pad material properties influence these responses. The experimental findings revealed that the pad material properties significantly affect the wear behavior and friction-induced vibration and noise responses of lightweight friction pairs. The pad enriched with lubricating phases (Pad A) readily established stable lubricating films, while the highly plastic pad (Pad C) effectively captured wear debris to build the third-body layers that cushioned loads. Both reduced friction fluctuations and contact stiffness, thereby attenuating vibration and noise. Conversely, the high-hardness pad (Pad B) failed to form continuous lubricating films, leading to intensified friction, higher contact stiffness, and pronounced vibration and noise. Numerical simulations further confirmed that the friction coefficient and normal contact stiffness synergistically regulated system stability, directly affecting the vibration and noise responses. Systems characterized by high friction and large contact stiffness (Pad B) were particularly susceptible to modal coupling, resulting in dynamic instability and elevated vibration and noise levels. Therefore, optimizing the pad material properties and regulating the behavior of wear debris to facilitate the stable formation of lubricating films or third-body layers can effectively suppress friction coefficient fluctuations, reduce normal contact stiffness, and enhance interfacial stability, thereby mitigating vibration and noise. The findings provide a theoretical foundation and engineering guidance for optimizing the design of low-noise lightweight braking systems and selecting appropriate friction materials.

Keywords: Synthetic brake pads; Aluminum matrix composite brake disc; Wear morphology; Vibration and noise; Normal contact stiffness

Just Accepted

1 Introduction

With the advancement of China's urban agglomeration strategy and the rapid development of an integrated transportation network, suburban railways have emerged as crucial transportation hubs linking the core areas of metropolitan regions to surrounding towns [1-3]. To meet the growing demand for cross-regional commuting, the operational speeds of suburban trains have steadily increased, with some lines designed for speeds of up to 160 km/h [4-6]. Nevertheless, the considerable increase in speed has significantly increased traction energy consumption [7], which presents a substantial technical challenge for suburban rail traffic systems in achieving a balance between energy efficiency and high-speed operation. Lightweighting of braking systems constitutes a critical strategy for reconciling rising operational speeds with traction energy demands by reducing unsprung mass and diminishing inertial losses in the traction system [8]. Reports have indicated that substituting conventional ferrous friction pairs with lightweight configurations composed of aluminum matrix composite(AMC) brake discs and synthetic brake pads can achieve weight reductions in excess of 50% [9], and for every 1 kg reduction in unsprung mass can save the traction energy consumption by roughly 0.065 kWh/km [8, 10]. For a six-car size train set, such reductions correspond to annual electricity savings of approximately 50,000 kWh and an associated carbon emission reduction of about 50 tonnes [11, 12], demonstrating significant effects on energy conservation and emission reduction. Furthermore, the lightweight braking systems also have significant advantages in enhancing vehicle dynamic responsiveness, improving wheel–rail interaction, and reducing life-cycle operation and maintenance costs [13, 14]. Although such considerable benefits are offered by lightweight technology, the inherent limitations of the lightweight friction materials remain evident. These materials typically have low stiffness, limited thermal capacity, and inadequate wear resistance, and are prone to interface instabilities under complex operating conditions, resulting in strong nonlinear vibration and noise (Fig. 1) [15-17]. Such deficiencies not only impair passenger comfort but also accelerate structural fatigue, thereby threatening braking safety [18, 19]. Accordingly, systematic investigation of the vibration and noise characteristics of lightweight friction pairs, together with elucidation of the underlying mechanisms, is crucial for enabling the design of braking systems that combine low noise, reduced vibration, and high reliability.

Just Accepted

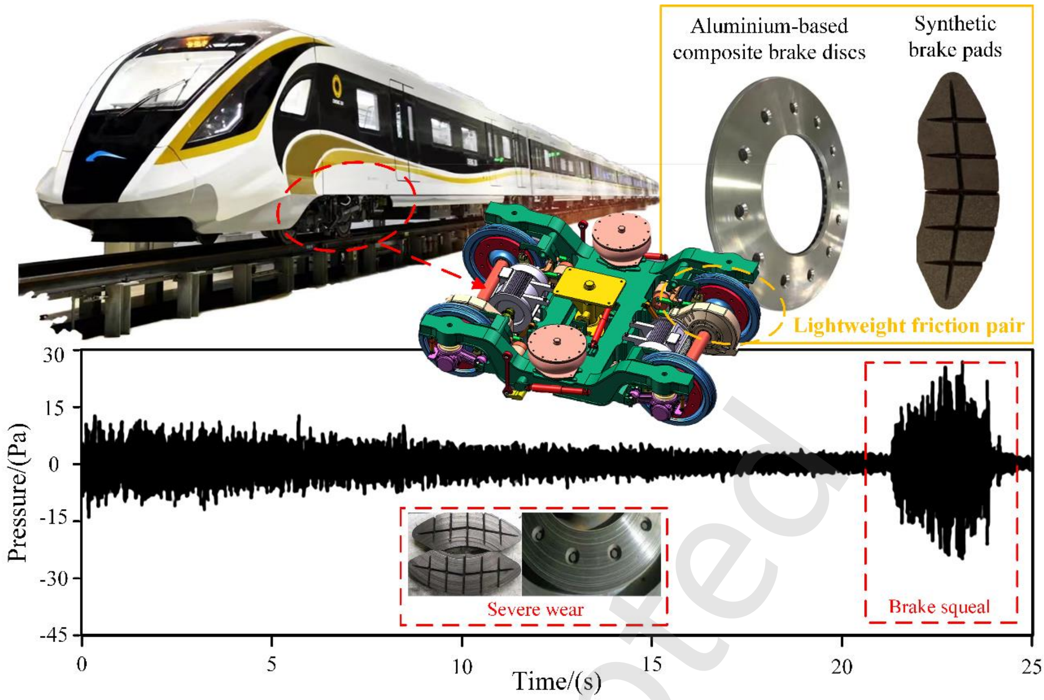

Fig. 1 Wear and brake noise problem in lightweight friction pairs for suburban trains.

Current research on lightweight friction pair materials primarily centers on their service reliability under braking conditions, with emphasis on evaluating their wear resistance and thermal stability[20-22]. For instance, Tan et al. [23] conducted 1,000 repeated braking tests on hybrid composite brake discs in an urban rail environment, systematically assessing their wear resistance and frictional stability. Baig et al. [24] and Pole et al. [25] investigated the influence of particle reinforcement type and proportion on the frictional behavior of composite materials. Nong et al. [26] employed a fluid–solid coupling approach to analyze the thermal behavior and stress distribution of aluminum-based composite brake discs under 350 km/h emergency braking. Song et al. [27] established the safe operational temperature range for these lightweight braking materials through thermal cycling tests. Collectively, these studies lay a foundation for understanding the reliability of lightweight friction pairs; however, they largely concentrate on material performance, with relatively limited focus on vibration and noise phenomena induced by their application. With vibration and noise issues of lightweight friction pairs becoming increasingly prominent in actual service, several researchers have begun to focus on these challenges. For instance, Cao et al. [28] investigated the braking noise of lightweight friction pairs in a metro vehicle through track tests and multi-modal simulation, demonstrating that both the friction coefficient and elastic modulus significantly influence noise. By selecting composite brake pads with moderate elastic modulus, the braking noise was effectively suppressed. Yang et al. [29] using the finite element complex eigenvalue analysis, further identified key factors influencing braking noise in lightweight friction pairs for urban rail vehicles, and pointing out that friction pairs composed of different materials have significant differences in vibration and noise performance. Although these studies offer preliminary insights into how material pairing affects vibration noise, they largely rely on specific simplified models and do not systematically investigate the mechanisms by which different composite brake pad materials regulate system vibration through interfacial wear evolution, particularly lacking cross-scale analyses that connect microscopic morphology with macroscopic vibration responses.

In studies of conventional braking material systems, the intrinsic coupling between interfacial tribological behavior and system dynamic response has been systematically explained [30, 31], providing a crucial foundation for understanding the tribological mechanisms of braking noise. For instance, Wei et al. [32] demonstrated that the impact of braking conditions on squeal noise is governed by the contact plateau morphology of friction materials. Shin et al. [33] and Lazim et al. [34] found that the size of abrasive particles governs the evolution of the surface friction layer, interfacial contact stiffness, and the time-dependent behavior of the friction coefficient, thereby directly affecting system instability. Hetzler et al. [35] introduced interface wear morphologies reconstructed via fractal theory into numerical models, establishing links between morphological features and system instability. Xiang et al. [36] further identified variations in the interface contact angle under different rotational speeds and systematically analyzed the relationship between contact inclination and vibration response using finite-element methods. However, current research primarily addresses differences in the vibration response of the same friction pair under varying operating conditions caused by changes in

Just Accepted

interfacial friction behavior [37-39], while systematic comparisons across different material combinations remain scarce. This makes it difficult to elucidate the generation mechanism of vibration and noise in different lightweight friction pairs, and also fails to provide effective guidance for material selection and adaptation. Furthermore, these conclusions are largely derived from conventional braking material systems with high stiffness and wear resistance, and their validity and applicability to lightweight friction pairs remain to be verified. In lightweight friction pairs with lower stiffness and limited wear resistance, interfacial contact parameters exhibit more pronounced variations during braking, resulting in highly random and complex vibration noise behavior across different material combinations [40], which significantly complicates material selection. Therefore, a cross-scale "material–interface–system" analytical framework is warranted to systematically investigate the mechanisms of vibration noise in lightweight friction pairs and to establish material selection criteria for low-noise design.

To further elucidate the mechanisms underlying vibration and noise in lightweight friction pairs, the study investigates three representative synthetic brake pads used in suburban trains, and the AMC brake discs as the counterparts, incorporating systematic tribological testing, interfacial morphology analysis, and fractal modeling. Initially, a thorough assessment of friction-induced vibration and noise characteristics is made possible by using the friction test apparatus to get the friction coefficient, vibration acceleration, and sound pressure signals for various friction pair combinations. Subsequently, scanning electron microscopy (SEM) and white light interferometry are used to analyze the morphology of interfacial wear to identify significant differences in contact behavior. Additionally, microstructural interface features are reconstructed based on fractal theory, and a two-degree-of-freedom disc–pad dynamic model incorporating variations in interfacial parameters caused by the materials is established to examine the influence of different material interface behaviors on system vibration response. This study constructs a material–interface–system framework for analyzing vibration and noise to systematically uncover the intrinsic relationship between the material properties

Just Accepted

of the synthetic brake pad and the vibration and noise response of the system. The findings help to make up for the shortcomings of current theories in the adaptability and dynamic response prediction of lightweight friction pairs and provide a scientific basis for material selection and design optimization in low-noise lightweight brake systems.

2 Experiment

2.1 Experimental equipment

To systematically investigate the friction-induced vibration and noise characteristics of different lightweight friction pairs, the friction tests were performed using the CETR UMT-3 tribological testing machine on three commercial synthetic pads and the AMC brake discs. The test setup and sensor configuration are depicted in Fig. 2. The apparatus enables precise multi-parameter control and high-frequency dynamic response acquisition. It can achieve constant-speed rotation of the brake disc through the rotational driving device, and the two-dimensional moving stage allows precise adjustment of the contact radius and normal force between the disc and the pad. During testing, the two-dimensional force sensor continuously recorded normal and tangential forces at the interface. A three-dimensional accelerometer mounted on the pad fixture captured vibration signals induced by friction, while a microphone placed directly in front of the disc–pad contact region recorded noise signals throughout the experiment. All signals were synchronously sampled at 10 kHz using the signal acquisition and analysis system to ensure the accurate detection of high-frequency vibration and noise characteristics. All experiments were conducted under standard atmospheric pressure, with ambient temperatures of 23-27 °C and relative humidity of 60 ± 10 %.

Just Accepted

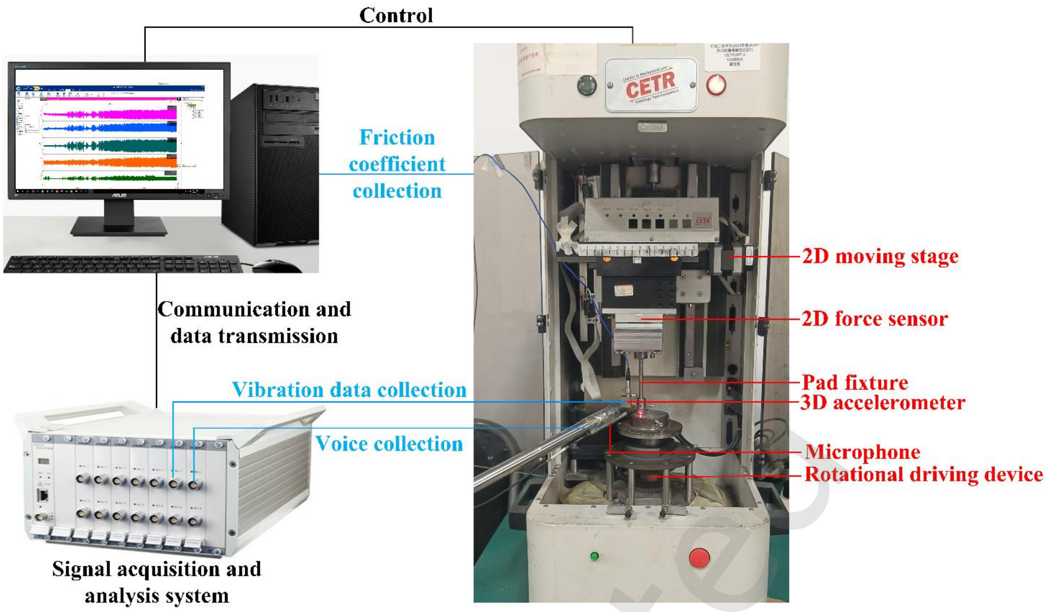

Fig. 2 Schematic diagram of test setup and sensor configuration.

2.2 Experimental materials

Three typical commercial synthetic brake pads in suburban train braking systems and the AMC brake discs were selected as the research objects, with the genuine samples displayed in Fig. 3(a). The synthetic brake pads were machined into cylindrical specimens with a diameter of 10 mm and a height of 17 mm, which were designated as Pad A, Pad B, and Pad C, respectively. The discs were fabricated from the AMC material, which had a diameter of 50mm and a thickness of 10mm. The disc–pad contact arrangement during testing is depicted in Fig. 3(b), with the contact radius of 17.5 mm.

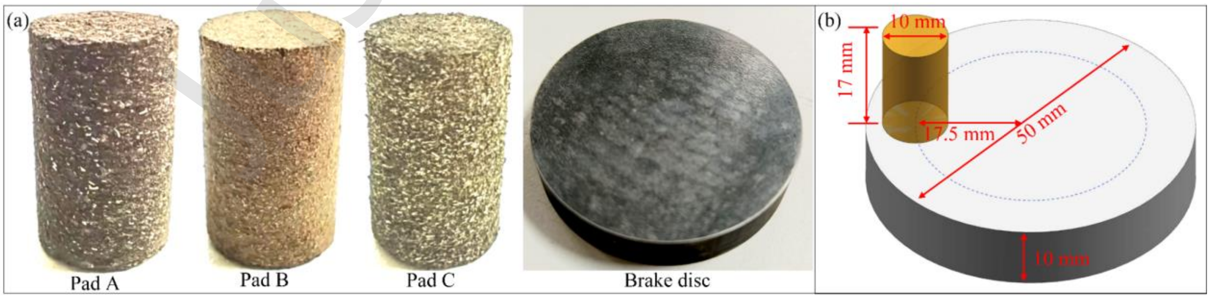

Fig. 3 The synthetic brake pads and the brake disc samples: (a) Physical diagram, (b) Test dimensions and contact diagram.

The three synthetic brake pads exhibited distinct differences in formulation and material properties, with their chemical compositions detailed in Table 1, and the essential physical parameters shown in

Table 2. As can be seen from the tables, Pad A is characterized by high carbon and titanium content, combined with relatively low density and hardness. Pad B contains moderate carbon and iron content, exhibiting higher hardness and compressive modulus, and strong interfacial load-bearing capacity. Pad C contains elevated levels of calcium and iron, with a relatively higher density but the lowest hardness and compressive modulus, reflecting substantial plastic deformation potential. The variations in composition and material properties establish the chemical and physical basis for the pads' differing friction, vibration, and noise behaviors in practical service. The aluminum matrix composite is primarily composed of Al, C, O, and Si elements. It exhibits a hardness of 869.8 HV and an elastic modulus of 102 GPa, which are substantially higher than those of the three synthetic brake pads [40].

Table 1 Chemical compositions of three synthetic brake pads and the brake disc.

Elements	C	O	Fe	Ca	Si	Ti
Pad A (wt%)	56.8	25.6	2.7	9.7	-	5.2
Pad B (wt%)	54.1	29.7	6.4	6.1	2.2	-
Pad C (wt%)	49.5	28.7	7.4	14.4	-	-

Table 2 Main material properties of three synthetic brake pads and the brake disc.

Type	Density (g/cm^3)	Hardness (HRX)	Compression modulus (MPa)
Pad A	2.02	22	194
Pad B	2.25	62.2	647
Pad C	2.30	21.4	120

2.3 Experimental method and characterization

All brake disc and synthetic brake pad specimens were mechanically polished and ultrasonically cleaned before testing to establish consistent initial interface conditions. The disc–pad contact was subsequently stabilized through an extensive running-in process. Given that vibration noise is more easily triggered during the low-speed phase near train stopping [39], the experiments were designed to simulate the response characteristics of lightweight friction pairs under such conditions. The disc–pad normal force was set at 40 N, corresponding to a typical operational braking pressure of 0.5 MPa, and

Just Accepted

the brake disc rotational speed was set at 200 r/min, equivalent to a train speed of 2.3 km/h. Each test lasted 30 minutes, during which synchronous acquisition of the friction coefficient, vibration acceleration, and noise signals was performed. To ensure reproducibility and statistical reliability, each test was repeated four times, with data from the stabilized stage selected for analysis. After testing, the white-light interferometry, scanning electron microscopy (SEM), and energy-dispersive spectroscopy (EDS) were employed to examine the friction interface morphology and elemental composition, providing support for revealing the intrinsic relationship between lightweight friction pair materials and interfacial behavior characteristics and vibration and noise behavior.

3 Experimental results and analysis

3.1 Dynamic response characteristics

3.1.1 Friction coefficient

Statistical analysis of the friction coefficients for the three lightweight friction pairs during the 120-160 s interval of the friction test is presented in Fig. 4. As shown, the friction pair composed of Pad A exhibits a relatively low average friction coefficient of 0.3, with minor fluctuations, indicating a stable interfacial friction process. In contrast, the friction pair composed of Pad B shows the highest average friction coefficient of 0.47, accompanied by significant fluctuations, which suggests an unstable friction state at the interface. Meanwhile, the friction pair composed of Pad C displays an intermediate average friction coefficient with low fluctuation amplitude, demonstrating superior frictional stability.

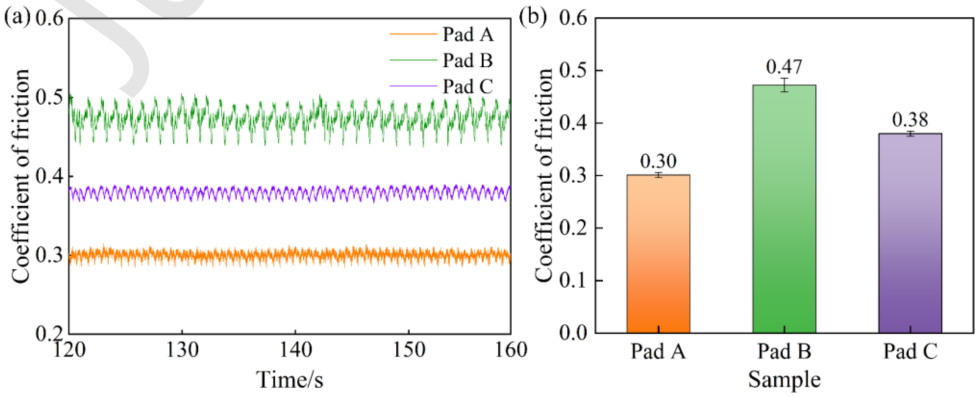

Fig. 4 Friction behavior of three lightweight friction pairs composed of three synthetic brake pads:

Just Accepted

(a) Friction coefficient curve, (b) Average value.

3.1.2 Vibration and noise

A further detailed examination of the vibration acceleration signals from 137 to 142 s reveals highly consistent characteristics in the time-frequency domain across the three directions, with the tangential component presenting significantly higher amplitude than the radial and normal components. This observation indicates that the system vibration is chiefly driven by tangential frictional excitation, highlighting the importance of focusing on the characteristics of the acceleration signal in this direction, as presented in Fig. 5. The friction pairs composed of Pad A and Pad C exhibit relatively low tangential acceleration amplitudes (Fig. 5(a) and 5(c)), with the root mean square (RMS) values of 3.30 mm/s^2 and 5.53 mm/s^2, respectively. The time-domain vibration signals of both pairs exhibit periodic fluctuations with small amplitudes, and their frequency components are primarily concentrated below 1000 Hz, indicating relatively stable response characteristics. The friction pair composed of Pad B displays a substantially larger tangential acceleration amplitude, with an RMS value of 50 mm/s^2 (Fig. 5(b)), characterized by distinct intermittent fluctuations. And the fluctuation period is highly consistent with the variation period of its friction coefficient (Fig. 4(a)), indicating a strong correlation between system vibration response and interfacial friction state. Spectral analysis further demonstrates that the periodic excitation of the friction interface is concentrated near 946 Hz, which induced significant vibration responses at the fundamental frequency and its harmonics.

Just Accepted

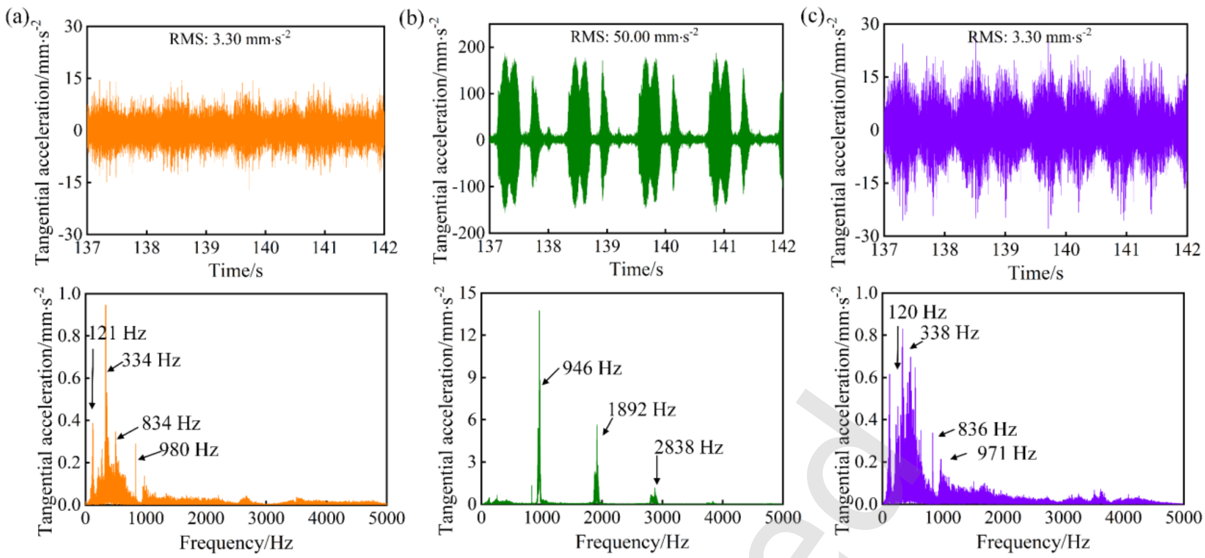

Fig. 5 Time and frequency domain tangential vibration acceleration signals of three lightweight friction pairs composed of: (a) Pad A, (b) Pad B, (c) Pad C.

Fig. **6** illustrates the time-domain noise signals and corresponding time-frequency spectrograms of the three lightweight friction pairs over the same time interval. The friction pair composed of Pad B radiates pronounced noise driven by strong interface-induced vibrations. Its acoustic pressure signal exhibits periodic fluctuations that align closely with the vibration response, while the spectrogram reveals distinct high-energy concentration zones within the same frequency range. The A-weighted equivalent sound pressure level reaches 82.46 dB(A), markedly exceeding those of the other two friction pairs. In comparison, the friction pairs composed of Pad A and Pad C are weaker and easily masked by background noise. The corresponding sound pressure signals show similar amplitudes without periodic features consistent with either the friction coefficient or vibration signals. Furthermore, no high-energy concentration regions are observed in their time-frequency spectrograms, further confirming the superior acoustic performance of these two lightweight friction pairs.

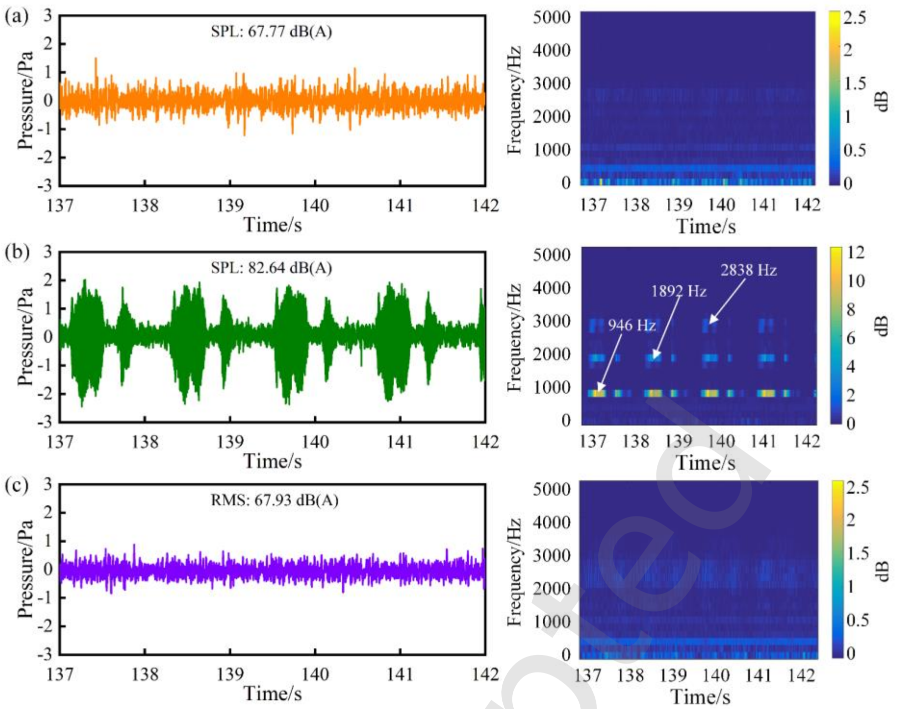

Fig. 6 Time domain and time-frequency diagrams of the noise of three lightweight friction pairs composed of: (a) Pad A, (b) Pad B, (c) Pad C.

The comprehensive analysis of the performance of friction, vibration and noise of the lightweight friction pairs shows that the amplitude and periodic evolution of the vibration and noise response are closely aligned with the variation in the friction coefficient, consistently exhibiting the trend of Pad B > Pad C > Pad A. This alignment provides strong evidence of the intrinsic correlation between interfacial friction and the system's dynamic behavior. Specifically, the significantly higher hardness of Pad B compared to the other two pads results in stronger load-bearing and micro-cutting effects during contact, resulting in a noticeable increase in the friction coefficient and inducing stronger vibration and noise. In addition, existing studies have pointed out that the friction coefficient with high amplitude and severe fluctuations introduces greater energy input into the interface, thereby promoting unstable vibrational behavior of the system[41, 42]. Thus, it can be inferred that material hardness serves as a critical factor governing vibration and noise behavior by altering interfacial contact states and energy input dynamics.

Just Accepted

3.2 Interface morphology analysis

Tribological test results demonstrate that the lightweight friction pairs composed of three synthetic brake pads exhibit pronounced variations in vibration and noise behavior, indicating that the material properties of the synthetic brake pads substantially affect the system dynamic responses by regulating the interfacial friction behavior. Therefore, it is necessary to characterize the wear morphology of lightweight friction pairs to analyze the differences in interface wear state and contact characteristics of the lightweight friction pairs, and then reveal the microscopic interface mechanism that causes the differences in the friction and vibration behavior of lightweight braking systems.

3.2.1 Surface wear morphology of the composite brake pads

Fig. **7** illustrates the SEM images of the wear areas of the three synthetic brake pads and the elemental composition of their principal constituents. As shown in Fig. 7(a), Pad A contains a substantial proportion of rod-shaped reinforcement materials, with the major elements of C, O, Si, Al, and Ca (Fig. 7(a-1)). These reinforcements have a certain stiffness, and their special rod-shaped morphology facilitates the formation of stable contact regions at the interface, thereby enhancing local load-bearing capacity. The presence of wear traces on the reinforcement surfaces further confirms their active participation in the interfacial wear process. Furthermore, the dispersed distribution of the rod-shaped reinforcements alleviates local stress concentrations and modulates the distribution of contact stiffness [43]. Additionally, a significant amount of graphite phases is uniformly distributed on the pad surface, accompanied by abundant carbon elements detected in the wear debris (Fig. 7(a-2)), indicating extensive involvement of graphite in the interfacial contact. The excellent lubricating properties of graphite contribute to reducing interfacial shear forces, stabilizing frictional behavior, and maintaining a relatively low friction coefficient [44, 45].

The surface of Pad B exhibits pronounced wear features, with fractured metallic materials and extensive accumulations of bright white hard particles observed in certain regions (Fig. 7b). Elemental analysis reveals that, besides Fe, the metallic materials contain a considerable amount of Si (Fig. 7(b-

Just Accepted

1)), indicative of their relatively high hardness. The bright white wear debris is not only rich in metallic constituents but also contains a high level of carbon. However, the wear debris of Pad B does not form a continuous lubricating film, and the lubrication effect is therefore limited (Fig. 7(b-2)). Such harder metallic phases in Pad B and the non-uniform dispersion of hard particles across the interface generate pronounced mechanical coupling effects, which disrupt the continuity and uniformity of interfacial contact. Consequently, the friction coefficient is elevated and exhibits strong fluctuations, and the contact stiffness is prone to substantial variation [46, 47].

The surface of Pad C contains large areas of metallic materials, in which the Si content is significantly reduced, leading to lower overall hardness and shear resistance of the metallic material (Fig. 7c). Despite this, the relatively high plastic deformability allows the surface of the friction block to maintain structural integrity under compaction, without apparent tearing (Fig. 7(c-1)). It indicates that interfacial mechanical interlocking and micro-cutting effects are comparatively weak, thereby alleviating interfacial shear stress and preventing the generation of excessive frictional forces. In addition, only limited graphite phases are observed on the pad surface, and the carbon content in the wear debris is markedly reduced (Fig. 7(c-2)), consistent with the low graphite fraction in the base material, which indicates that the lubricating effect of graphite at the interface is comparatively weak. Nevertheless, portions of the compacted wear debris form locally stable third-body structures that reduce interfacial shear forces and redistribute stress concentrations [48], thereby lowering and stabilizing the friction coefficient. The interface also contains numerous micro-cracks arising from localized stress concentrations, which help to mitigate load fluctuations and suppress sudden variations in frictional force. Through the combined action of the above interfacial features, the synthetic brake pad achieves a moderate yet stable frictional performance output.

Just Accepted

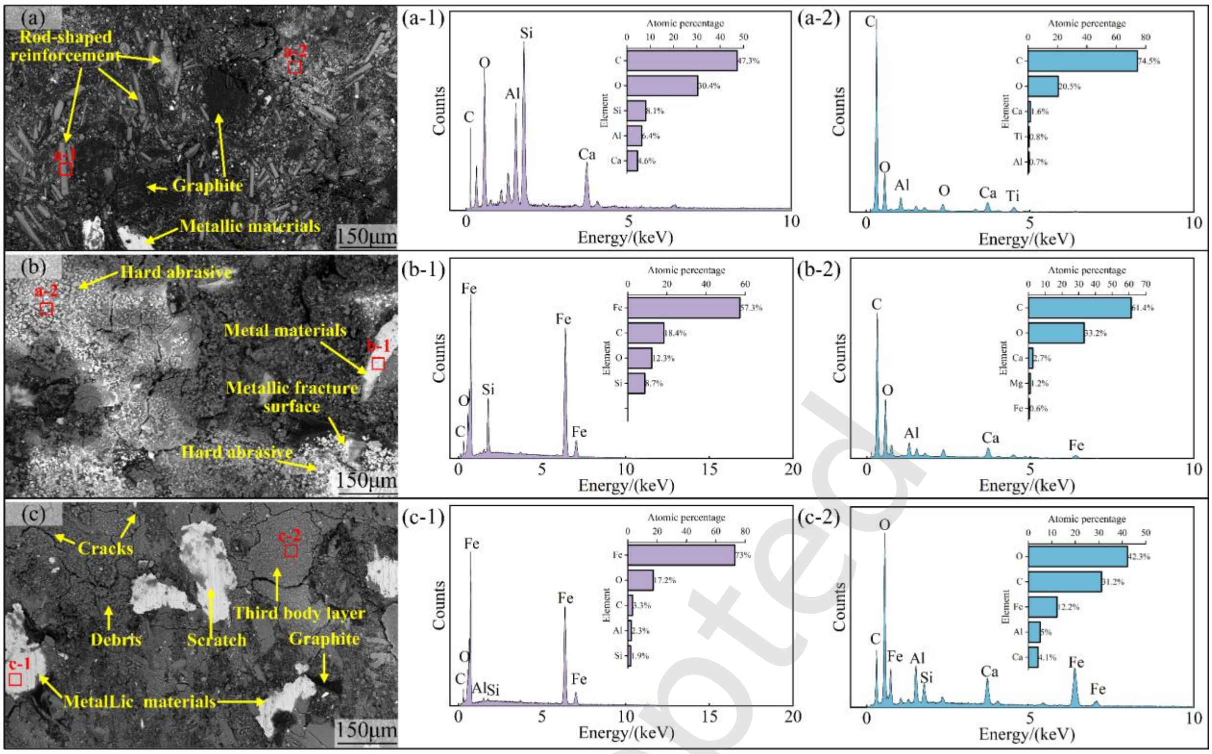

Fig. 7 SEM and EDS analysis of the synthetic brake pads surface: (a) Pad A, (b) Pad B, (c) Pad C.

A further analysis of the three-dimensional surface morphology and two-dimensional contour profiles of the three synthetic brake pads is presented in Fig. 8. The surface of Pad A is primarily composed of extensive contact plateaus and localized spalling pits, exhibiting a moderate roughness level (Fig. 8(a)). The contact plateaus sustain the majority of the load during friction and give rise to stable contact regions [49]. Such regions facilitate the development of a continuous and stable load-bearing surface, which in turn suppresses pronounced fluctuations in the micro-contact state. For Pad B, the relatively high hardness and compressive modulus enable it to accommodate external loads effectively, leading to only minor surface wear and a comparatively smooth topography (Fig. 8b). This morphology enlarges the real contact area and substantially increases contact stiffness. The intermittent grooves oriented along the sliding direction are also evident, indicating that the interface underwent pronounced shear wear or abrasive plowing (Fig. 8b), which contributed to higher frictional resistance. Meanwhile, the high hardness and limited plastic deformability of the pad, the interface more vulnerable to producing unstable contact and localized slip, ultimately inducing drastic fluctuations in

Just Accepted

the friction coefficient at a high level. For Pad C, the surface exhibits large-scale depressions and spalling pits in localized regions, leading to reduced flatness and a comparatively high surface roughness of *Ra*=3.43 μm (Fig. 8c). These morphological features arise primarily from the low hardness of the matrix material and the limited load-bearing capacity of the interfacial metallic phase, which makes the material prone to deformation and spalling during sliding. Nevertheless, the favorable plastic deformability of the material plays an important role in mitigating shear fluctuations and stabilizing the interfacial mechanical response.

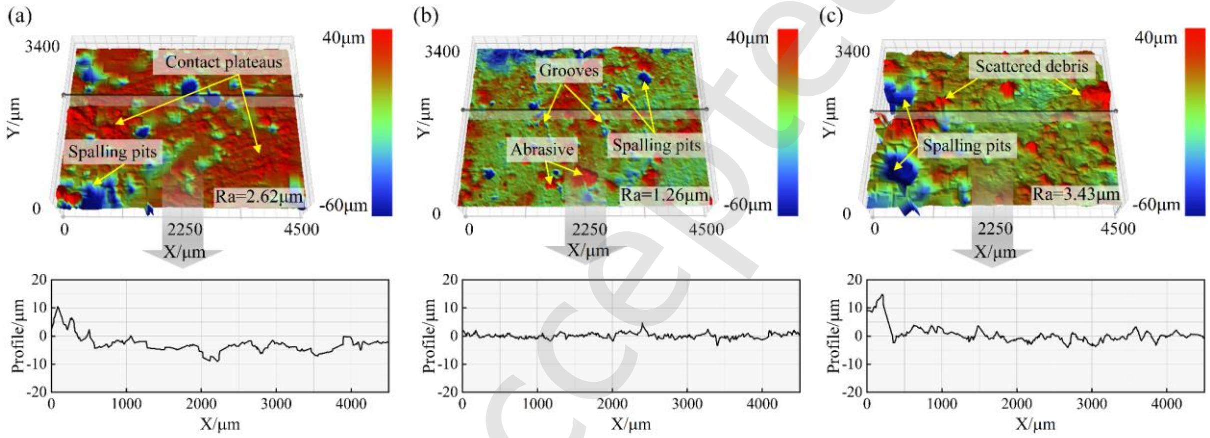

Fig. 8 3D morphology and 2D contour profiles of the synthetic brake pad surfaces: (a) Pad A, (b) Pad B, (c) Pad C.

3.2.2 Surface wear morphology of the brake discs

Fig. **9** illustrates the wear morphologies and EDS analysis results of the original brake disc surface and the brake disc surfaces after testing against different synthetic brake pads. As shown in Fig. 9(a), the original brake disc surface is smooth and free of noticeable scratches or deposits. EDS analysis further confirms that the original brake disc is predominantly composed of Al, Si, O, and C. The brake disc surface after testing against Pad A exhibits no evident scratches but shows an accumulation of carbon-rich wear debris (Fig. 9(b)), indicating that the graphite phases from the pad were transferred and adhered to the disc, thereby forming a transfer film. The presence of the transfer film helps improve the interfacial lubrication state, mitigates severe contact fluctuations [50], and consequently maintains relatively low levels of friction coefficient and vibration response. The brake disc surface after testing against Pad B displays pronounced scratches with hard particles embedded in localized areas (Fig. 9(c)), reflecting aggressive wear behavior characterized by elevated contact stiffness and concentrated stress distribution. The brake disc surface after testing against Pad C is covered by a certain thickness of wear debris retained on the surface without penetrating the substrate (Fig. 9(d)), which indicates insufficient interfacial contact stiffness. The debris accumulation on the disc surface contributes to the suppression of frictional disturbances and thereby enhances the stability of the friction-induced vibration response.

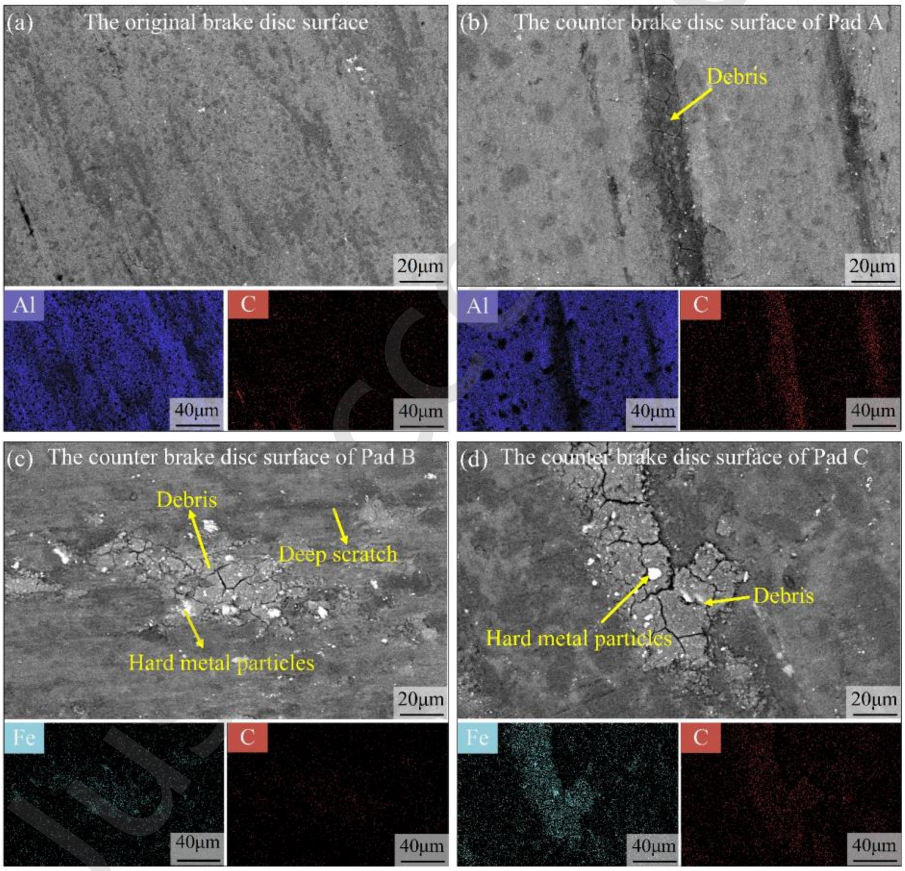

Fig. 9 SEM images and EDS analysis of the brake disc: (a) original brake disc surface, (b) brake disc surface after testing against Pad A, (c) brake disc surface after testing against Pad B, and (d) brake disc surface after testing against Pad C

In summary, due to the intrinsic material characteristics of the synthetic brake pads, the interfacial behaviors of the three lightweight friction pairs during the friction process exhibit significant differences, primarily involving multiple regulatory mechanisms such as transfer film formation, hard-particle abrasion, and plastic buffering of the substrate. Such interfacial behaviors directly affect the magnitude and stability of the friction coefficient, while the resulting differences in surface morphology alter load distribution and consequently affect the contact stiffness response under external loads [49]. However, there is still a lack of systematic research on the mechanism of the changes in interface friction coefficient and contact stiffness caused by the interface friction and wear behavior of different synthetic brake pads on the vibration and noise behavior of lightweight friction pairs. Therefore, it is imperative to establish a coupled analytical framework that integrates interfacial wear morphology, interfacial parameters, and system response characteristics to clarify the vibration and noise generation mechanisms in lightweight friction pairs from a tribological perspective.

4 Dynamic simulation analysis

To elucidate the influence of different material interfacial behaviors on system vibration dynamics, a two-degree-of-freedom disc–pad dynamic model considering the changes in interface parameters was established, and the numerical simulation analysis was carried out. Specifically, the microscopic interfacial morphologies of different synthetic brake pads were reconstructed based on fractal theory to evaluate contact stiffness. Subsequently, the contact stiffness, in conjunction with the friction coefficient obtained from tribological experiments, were incorporated as the pivotal input parameters into the dynamic model. Then, the stability boundaries and dynamic response characteristics of the system under varying interfacial conditions were systematically investigated, thereby revealing the critical mechanisms of vibration and noise generation and clarifying the intrinsic coupling between pad material properties and system-level vibration responses.

4.1 Establishment of the brake disc–pad dynamic model

To qualitatively elucidate the system stability characteristics corresponding to specific combinations of friction coefficient and contact stiffness in friction pairs, a disc-pad dynamic model was developed, as shown in Fig. 10, and analyzed within a linear system framework. Damping was omitted to avoid potentially concealing critical instability mechanisms, thereby enabling the model to effectively

Just Accepted

capture the instability boundaries and their evolution under given combinations of friction coefficient and normal contact stiffness. In this model, the disc–pad contact behavior is simplified into a dynamic interaction between a mass block and a moving belt. To more faithfully represent the tribological behavior of different synthetic brake pads, the model incorporates experimentally acquired surface morphology data to construct interfacial profile features that closely replicate the actual contact state. This refinement enables accurate characterization of the interfacial normal contact stiffness and friction coefficient for various material pairings. Within the model, $k_i\left(i=A,B,C\right)$ denote the normal contact stiffness between the three synthetic brake pads and the AMC brake disc, which are determined by the specific interfacial morphology [51] and would be calculated in Section 3.2 subsequently. F_f is the interfacial friction, expressed as $F_f=-\mu_i k_i y$. $\mu_i\left(i=A,B,C\right)$ represent the measured friction coefficients of the different synthetic brake pads. Given that the dynamic model established in this study is intended for linear stability analysis, which examines the system's dynamic characteristics under steady-state conditions, the average value of the time-varying friction coefficient is employed as the system input, with the specific value of $\mu_A=0.3, \mu_B=0.47, \mu_A=0.38$, respectively. The quality of the mass block is m, and the velocity of the conveyor belt is v. Two linear springs (k_1 and k_2) with angles of α_1 and α_2 are applied to constrain the motion of the mass block.

Just Accepted

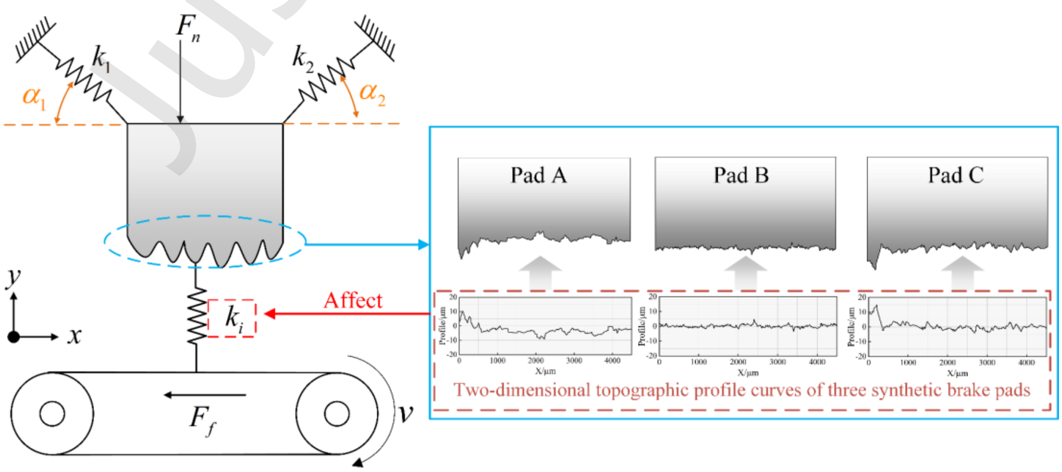

Fig. 10 Brake disc-pad dynamic model.

The kinetic equation of the model is:

$$\begin{cases} m\ddot{x}+\left(k_1\cos^2\alpha_1+k_2\cos^2\alpha_2\right)x+\left(-k_1\sin\alpha_1\cos\alpha_1+k_2\sin\alpha_2\cos\alpha_2\right)y=F_f \\ m\ddot{y}+\left(-k_1\sin\alpha_1\cos\alpha_1+k_2\sin\alpha_2\cos\alpha_2\right)x+\left(k_1\sin^2\alpha_1+k_2\sin^2\alpha_2+k_i\right)y=-F_n \end{cases} \tag{1}$$

After linearizing the dynamic equations, the Jacobian matrix of the system is obtained as:

$$\mathbf{J}=\begin{bmatrix} 0 & 1 & 0 & 0 \\ -\dfrac{K_1}{m} & 0 & -\dfrac{K_2+\mu_i k_i}{m} & 0 \\ 0 & 0 & 0 & 1 \\ -\dfrac{K_2}{m} & 0 & -\dfrac{K_3}{m} & 0 \end{bmatrix} \tag{2}$$

where, $K_1=k_1\cos^2\alpha_1+k_2\cos^2\alpha_2$, $K_2=-k_1\sin\alpha_1\cos\alpha_1+k_2\sin\alpha_2\cos\alpha_2$, $K_3=k_1\sin^2\alpha_1+k_2\sin^2\alpha_2$.

4.2 Solution of normal contact stiffness

To accurately identify the normal contact stiffness of different lightweight friction pairs, a normal contact stiffness model for rough surfaces was constructed based on fractal theory [52]. Fractal theory holds that engineering surfaces generated by random processes exhibit multi-scale self-similarity. Accordingly, parameters of surface asperities, such as height, curvature radius, and contact area of asperities, also follow the fractal distribution laws and can be characterized by fractal dimension and fractal roughness [53]. Leveraging this principle, the prediction of interfacial contact stiffness can thus be formulated as a statistical integration problem. Specifically, by determining the contact characteristics of asperities and discerning their elastic or elastoplastic deformation states, the normal contact stiffness of the interface can be effectively calculated by statistically integrating the contact responses of asperities across different deformation states.

4.2.1 Fractal Characterization of Rough Surfaces

Accurate characterization of the interfacial morphology in different lightweight friction pairs constitutes a fundamental prerequisite for obtaining accurate contact performance parameters. To this end, the Weierstrass-Mandelbrot (W-M) function [54], which possesses intrinsic fractal properties, was employed to model the surface morphology of the interfacial contact region. This function has been

Just Accepted

widely adopted for fractal descriptions of complex rough surfaces and is regarded as possessing high physical fidelity and mathematical rigor [55, 56]. Referring to the W-M function, the height function of a three-dimensional isotropic surface profile can be formulated as [57]:

$$z(x,y)=L\left(\frac{G}{L}\right)^{(D-2)}\left(\frac{\ln\gamma}{M}\right)^{1/2}\sum_{m=1}^{M}\sum_{n=0}^{n_{\max}}\gamma^{(D-3)n}\left\{\cos\phi_{m,n}-\cos\left[\frac{2\pi\gamma^{n}\left(x^{2}+y^{2}\right)^{1/2}}{L}\times\cos\left(\tan^{-1}\left(\frac{y}{x}\right)-\frac{\pi m}{M}\right)+\phi_{m,n}\right]\right\} \tag{3}$$

where, $z(x,y)$ refers the surface morphology height at sampling point (x,y). L represents the sampling length. D and G denote the fractal dimension fractal roughness of the surface profile, respectively; γ denotes the scale parameter (usually set $\gamma=1.5$); M is the number\` of overlapping ridges on the rough fractal surface; $\phi_{m,n}$ is a random phase generated between $[0,2\pi]$; n is the frequency index; $n_{\max}$ is the upper limit of the frequency index, and its value satisfies $\gamma^{n_{\max}}=L/L_s$, where L_s is the instrument measurement resolution.

The continuous approximate power spectrum of the function $z(x,y)$ [58] can be written as:

$$S(\omega)=\frac{G^{2(D-1)}}{2\ln\gamma}\frac{1}{\omega^{(5-2D)}} \tag{4}$$

As a result, the log-log representation of the power spectrum with frequency shows a linear relationship when the logarithms on both sides of Eq. (4) are taken. The slope and intercept of this linear function may then be used to compute the fractal dimension D and fractal roughness G of the rough surface profile using the following expressions:

$$D=\frac{k+5}{2} \tag{5}$$

$$\log G=\frac{b+\log\left(2\ln\gamma\right)}{2\left(D-1\right)} \tag{6}$$

The above content outlines the fundamental principle of extracting fractal parameters using the power spectral density (PSD) method. To evaluate the suitability of the aforementioned isotropic surface model for the materials employed in this study, a two-dimensional power spectrum analysis

Just Accepted

was carried out on the three-dimensional worn surface morphologies of the three synthetic brake pads. As shown in Fig. 11, the power spectra of all surfaces exhibit pronounced axial symmetry, indicating that their microscopic morphologies are statistically quasi-isotropic [57]. This observation validates the applicability of the proposed fractal model for reconstructing the surface topographical features. On this basis, the PSD of the surface profiles for the different synthetic pads (Fig. 8) is calculated and plotted on a logarithmic scale(Fig. 12). A least-squares fit is applied to these logarithmic curves, from which the fractal parameters (D and G) are obtained using Eqs. (5) and (6) (see results in Table 3). Substitution of the determined fractal parameters D and G into Eq. (3) enables an accurate characterization of the 3D fractal surface topography for each pad.

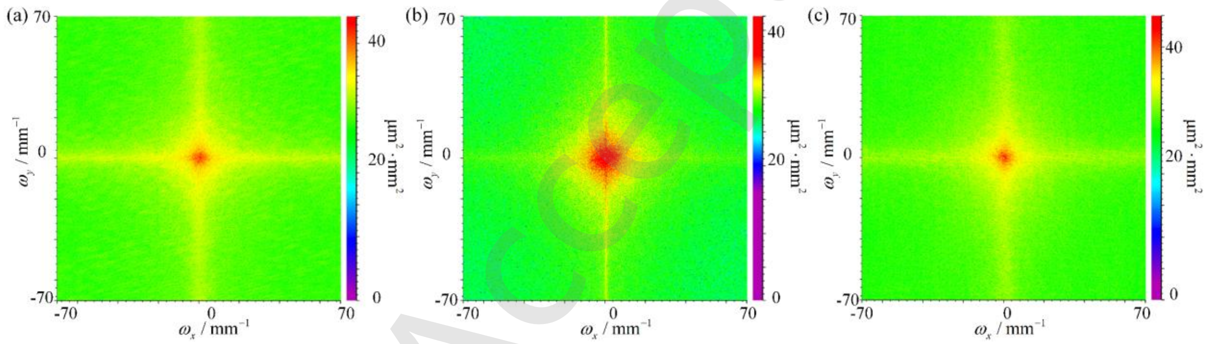

Fig. 11 2D power spectrum of the synthetic brake pad surfaces: (a) Pad A, (b) Pad B, (c) Pad C.

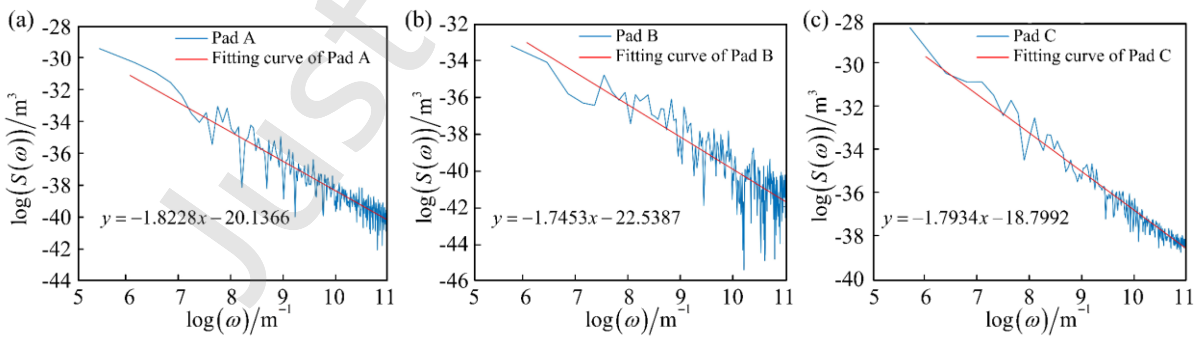

Fig. 12 Logarithmic power spectrum of the surface profiles of different synthetic brake pads: (a) Pad A, (b) Pad B, (c) Pad C.

Table 3 Fractal parameters of the surface profiles of the three synthetic brake pads.

Type	Slope k	Intercept b	Fractal dimension D	Fractal roughness G

Just Accepted

Pad A	-1.8228	-20.1366	1.5886	3.1179e-8
Pad B	-1.7453	-22.5387	1.6273	1.3367e-8
Pad C	-1.7934	-18.7992	1.6033	1.4392e-7

4.2.2 Model of Normal Contact Stiffness

Furthermore, a normal contact stiffness model was developed using the fractal function that captures the surface profile characteristics of different brake pads, enabling quantitative evaluation of normal contact stiffness across various lightweight friction pairs. Drawing on the equivalent contact principle of fractal theory, this study models the actual contact between the brake disc and the brake pad as the interaction between a fractal rough surface, described by the W-M function, and an ideal rigid plane. Within this framework, the brake disc is represented as a rigid plane due to its substantially higher hardness and stiffness and lower surface wear than that of the synthetic brake pad. As noted by Bhushan and Majumdar [59], when two contacting surfaces exhibit significant differences in hardness and roughness, the harder, less worn surface can be idealized as a rigid plane, while the softer, more heavily worn surface can be regarded as a fractal rough surface to calculate the contact stiffness of the interface. Finally, the disk-pad equivalent contact diagram is drawn as shown in Fig. 13.

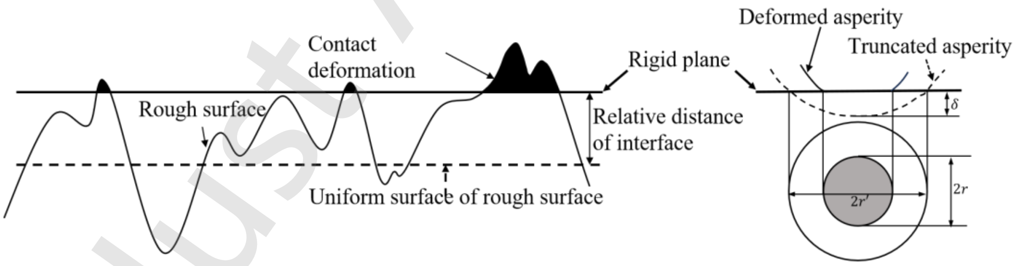

Fig. 13 Schematic diagram of the equivalent contact model of brake disc-pad contact.

The expressions for the contact deformation of an asperity δ and the elastic-plastic critical contact area of the asperity a_c' are [57]:

$$\delta = 2^{(4-D)} G^{(D-2)} \left(\ln \gamma\right)^{1/2} \pi^{(D-3)/2} a'^{(3-D)/2} \tag{7}$$

$$a_c' = \left[\frac{2^{(11-2D)}}{9\pi^{(4-D)}} G^{(2D-4)} \left(\frac{E^*}{H} \right)^2 \ln \gamma \right]^{1/(D-2)} \tag{8}$$

where R represents the asperity curvature radius. E^* denote the equivalent elastic modulus, with the expression of $E^* = \left[\left(1-\nu_1^2\right)/E_1 + \left(1-\nu_2^2\right)/E_2\right]^{-1}$. Among it, E_1, E_2 and ν_1, ν_2 correspond to the elastic modulus and the Poisso ratio of the two contact bodies, respectively. H is the hardness of the softer material in the contact bodies. When the condition $a' > a'_c$ is met, the contact bodies undergo elastic contact deformation, otherwise plastic deformation occurs. According to Eqs. (7) and (8), the critical contact area a'_c is affected by the elastic modulus and hardness of the contact bodies material. When the elastic modulus is low and the hardness is high, a'_c decreases.

Under the given normal force F_n, the maximum cut-off contact area of the asperity is [60]:

$$a'_L = \left(\frac{3F_n}{4E^* \pi^{1/2} G^{(D-1)} \gamma^{Dn_{\max}}} \right)^{2/3} \tag{9}$$

According to fractal theory, the size distribution function of the contact cross-sectional area of the asperity $n\left(a'\right)$ can be written as [57]:

$$n\left(a'\right) = \frac{\left(D-1\right)}{2a'_L} \left(\frac{a'_L}{a'} \right)^{(D+1)/2} \tag{10}$$

where, a' is the cross-sectional area of the asperity.

When $a'_L > a'_c$, the asperity undergoes elastic deformation and the corresponding elastic deformation force is [60]:

$$F_e = \frac{2^{(11-2D)/2}}{3\pi^{(4-D)/2}} \left(\ln \gamma\right)^{1/2} G^{(D-2)} E^* \left(a'\right)^{(4-D)/2} \tag{11}$$

On the contrary, the asperity undergoes plastic deformation, which does not provide an elastic deformation force. Thus, the normal contact stiffness of the entire rough contact surface can be described as:

$$K_n = \int_{a'_c}^{a'_L} \frac{dF_e}{d\delta} n(a')da' = \int_{a'_c}^{a'_L} \frac{2^{1/2}(4-D)(D-1)}{3\pi^{1/2}(3-D)} E^* (a'_L)^{(D-1)/2} (a')^{-D/2} da'$$
$$= \frac{2^{3/2}(4-D)(D-1)}{3\pi^{1/2}(2-D)(3-D)} E^* (a'_L)^{1/2} \left[1-\left(\frac{a'_c}{a'_L}\right)^{(2-D)/2}\right] \tag{12}$$

According to Eqs. (7) and (12), the normal contact stiffness of the rough contact surface is affected by the contact surface profile parameters of the brake pad (D and G), the elastic moduli of the contact bodies (E_1 and E_2), and the hardness H. Therefore, based on the derivation of the above equations, the influence trend of the synthetic brake pad material properties, specifically the elastic modulus E_2, hardness H, and the interface surface profile parameters (D and G) on the normal contact stiffness of lightweight friction pairs is clarified, as shown in Fig. 14.

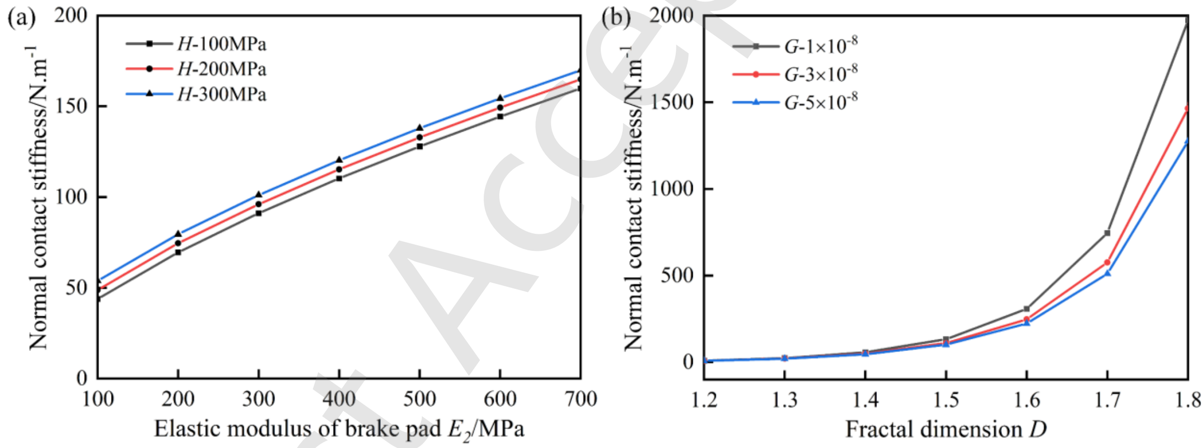

Fig. 14 Interface normal contact stiffness variation trend under the influence of: (a) Elastic modulus and hardness of the synthetic brake pad, (b) Fractal dimension and fractal roughness.

As illustrated in Fig. 14(a), the normal contact stiffness of the interface is more significantly impacted by the synthetic brake pad's elastic modulus than by the material's hardness. Normal contact stiffness only marginally rises with increasing hardness, but it increases steadily with increasing elastic modulus. As illustrated in Fig. 14(b), the effect of fractal roughness on normal contact stiffness is contingent on the fractal dimension. At low fractal dimensions, variations in fractal roughness have a minimal impact on contact stiffness. However, with increasing fractal dimension, contact stiffness

Just Accepted

increases exponentially, and the influence of fractal roughness becomes pronounced.

Similarly, the material parameters and contact morphology parameters of the three synthetic brake pads are substituted to obtain the normal contact stiffness of the three lightweight friction pairs, are $k_A = 138.23$ N/m, $k_B = 505.22$ N/m, $k_C = 83.08$ N/m, respectively.

4.3 Numerical Simulation Results and Analysis

The interface contact stiffness of different lightweight friction pairs identified above is integrated into the developed disc–pad dynamic model along with the friction coefficient obtained from the tribological test, to analyze the variation trends of the system vibration stability with the normal contact stiffness and friction coefficient, thereby revealing the influencing mechanisms of vibration noise behavior for different lightweight friction pairs. The simulation conditions are kept similar with the experimental setup, with the relevant parameters set as follows: $k_1 = 735$ N/m, $k_2 = 550$ N/m, α_1=45°, α_2=30°, $m = 0.03$ kg. The contact stiffness values of the two linear springs (k_1 and k_2) were calculated and solved by finite element static analysis, followed by equivalent conversion and fine-tuning. The angular parameters (α_1 and α_2) were configured with reference to representative values commonly employed in prior modeling studies [61].

The synthetic brake pads with different material properties significantly influence the interface friction coefficient and normal contact stiffness by regulating interfacial friction behavior. To investigate the mechanism of the effect of interface contact parameters on system stability, the Jacobian matrix and stability theory were employed to analyze the variation of system stability with friction coefficient and normal contact stiffness, thereby clarifying the relationship between brake pad material characteristics and system dynamics. Fig. **15** illustrates the real and imaginary parts (frequency) of the system eigenvalues under different conditions of normal contact stiffness and friction coefficient. When the friction coefficient exceeds 0.1, as the normal contact stiffness increases, the system progresses through three stages: stable, unstable (the modal coupling), and stable. Moreover, within

Just Accepted

the unstable region, the higher friction coefficient leads to a larger real part of the system eigenvalue, indicating a greater degree of system instability. The locations of the three synthetic pads are marked in the figure based on their measured friction coefficients and normal contact stiffness values. Pad A and Pad C are located within the stable region, while Pad B lies in the unstable region.

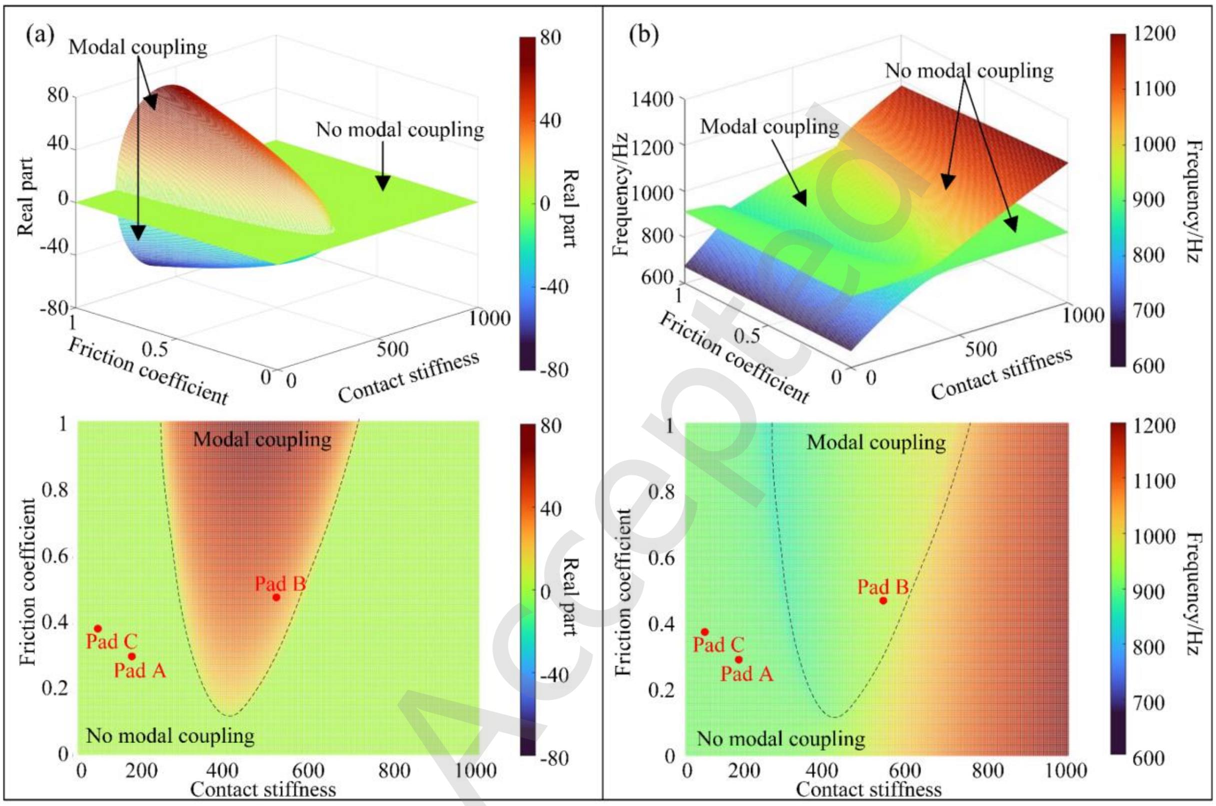

Fig. 15 The influence of friction coefficient and normal contact stiffness on the stability of friction systems: (a) Real part of eigenvalues, (b) Imaginary part of eigenvalues.

For Pad B, an additional analysis was performed by examining the variation of system eigenvalues with different friction coefficients under the corresponding normal contact stiffness of Pad B, as shown in Fig. 16. The results reveal that when the friction coefficient exceeds 0.315 the experimentally measured value of Pad B is 0.48), the real part of the eigenvalues bifurcates and the frequencies gradually converge, suggesting the occurrence of modal coupling and system instability. In addition, the frequency at which mode coupling occurs is 946 Hz, which coincides with the dominant vibration and noise frequency observed in the experimental tests of Pad B. This consistency demonstrates that the vibration and noise of the lightweight friction pair are induced by mode coupling, and confirms

Just Accepted

that the developed model can effectively capture the dynamic response at the brake disc–pad interface.

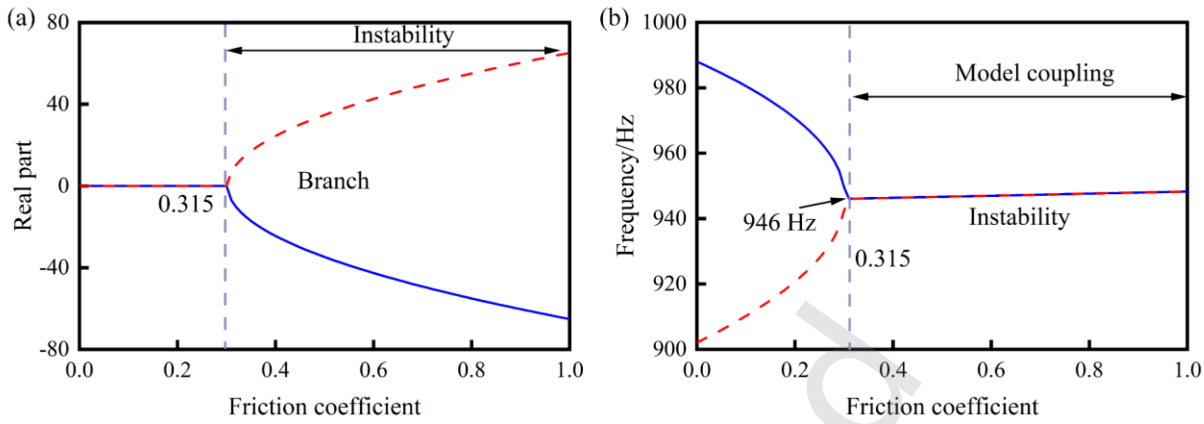

Fig. 16 The influence of the Pad B friction coefficient on system stability: (a) Real part of eigenvalues, (b) Imaginary part of eigenvalues.

Finally, numerical simulations were conducted to evaluate the time-domain responses of tangential velocity under varying interface contact parameters of the lightweight friction pairs, as shown in Fig. 17. The results demonstrate that Pad B exhibits the highest tangential velocity, followed by Pad C, whereas Pad A presents the lowest value, consistent with the vibration and noise trends identified in the tribological experiments. In conjunction with the system stability analysis, it can be concluded that the relatively high friction coefficient and normal contact stiffness of Pad B induce modal coupling and instability, thereby exciting pronounced friction-induced vibrations and radiating high-intensity noise. In contrast, Pad A and Pad C, characterized by comparatively lower friction coefficients and normal contact stiffness, remain stable without mode coupling, leading to more stable operation and a significant decrease in vibration amplitude. To synthesize, the generation mechanism of vibration and noise in different synthetic brake pads can be attributed to the coupling effect between the interfacial friction coefficient and normal contact stiffness, which alters the system stability. Specifically, the system becomes unstable under certain conditions due to the occurrence of modal coupling, resulting in high-frequency self-excited vibrations that trigger intense vibrations and squeal noise.

Just Accepted

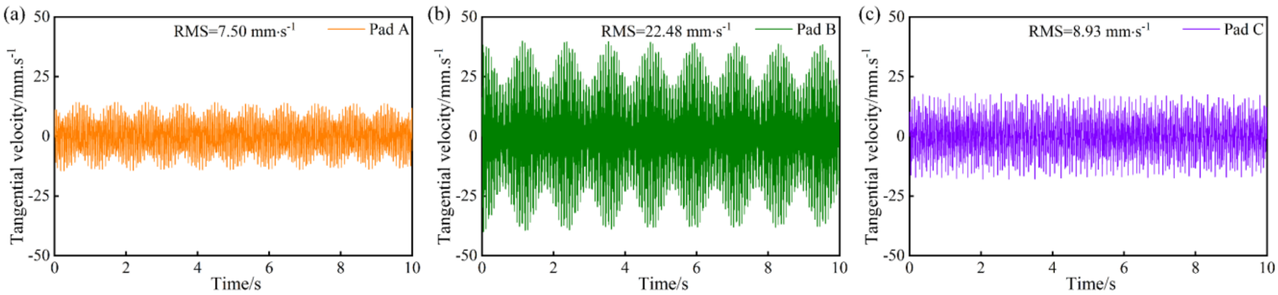

Fig. 17 Simulation results of the tangential velocity time domain signals of different synthetic brake pads: (a) Pad A, (b) Pad B, (c) Pad C.

5 Correlation mechanism between the material properties and vibration and noise behavior

Integrating tribological tests, interfacial morphology characterization, and dynamic simulations, this study identified the causes of the distinct vibration and noise behaviors among lightweight friction pairs with different synthetic brake pads and established the cross-scale correlation mechanism of "material–interface–system" as shown in Fig. 18.

Specifically, Pad A leverages the supporting function of its rod-like reinforcement phase together with the lubricating action of graphite to optimize load distribution at the interface and promote the formation of the stable lubricating film. Consequently, the interfacial friction coefficient remains low and exhibits only minor fluctuations. Owing to the relatively low compressive modulus and hardness of the material, the corresponding normal contact stiffness is also reduced. Under the combined influence of these factors, the system remains stable, resulting in small vibrations and noise. Although Pad C contains less lubricating phase, its enhanced plastic deformation capacity allows the wear debris to adhere at the interface, forming a localized and stable third-body structure that buffers load variations and stabilizes the friction coefficient. Together with its higher surface roughness and reduced hardness and compressive modulus, this further lowers the interfacial contact stiffness. Since the system does not reach the instability threshold, the overall vibration and noise response remains low. In contrast, Pad B demonstrates elevated levels of hardness and substantial load-bearing capacity, resulting in significant frictional interactions with the AMC brake disc. This process generates numerous hard wear particles on the surface, hindering the formation of a continuous lubricating film

Just Accepted

and giving rise to a higher and more unstable friction coefficient. Additionally, the high surface smoothness and large real contact area markedly increase the interfacial contact stiffness. Under the combined influence of the high friction coefficient and normal contact stiffness, the system undergoes mode coupling, enters the instability region, and consequently generates severe vibration and noise.

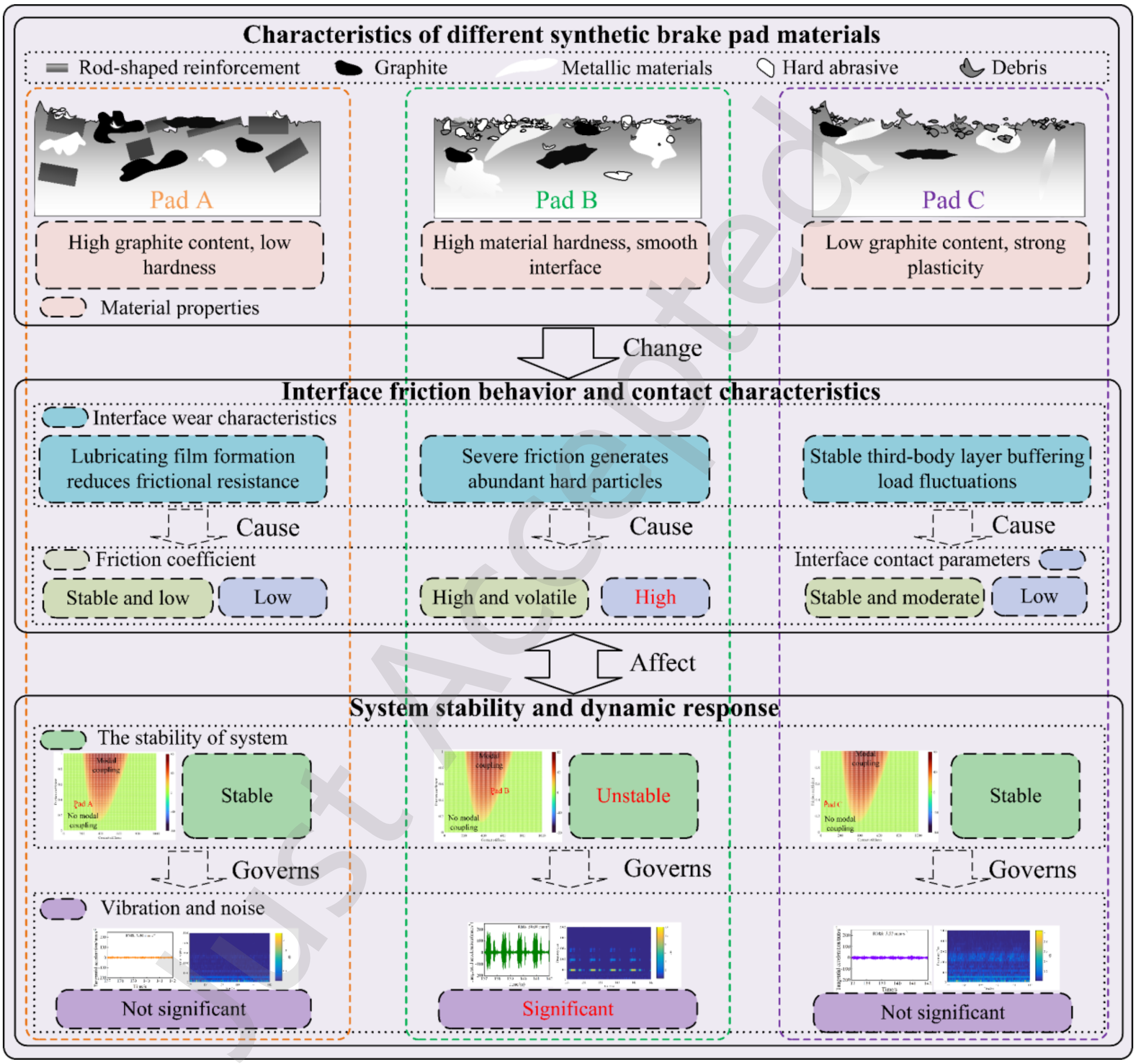

Fig. 18 The influence mechanism of vibration and noise behavior of the lightweight friction pairs.

In conclusion, the material properties of different lightweight friction pairs alter interfacial friction behavior and regulate the interfacial friction coefficient and contact stiffness, thereby changing system stability and vibration and noise characteristics. Overall, optimizing the material properties of the synthetic brake pads and regulating the behavior of wear debris to facilitate the stable formation of lubricating films or third-body layers can effectively suppress friction coefficient fluctuations, reduce normal contact stiffness, and enhance interfacial stability, thereby mitigating vibration and noise.

6 Conclusions

This work systematically evaluated the vibration and noise responses of lightweight friction pairs composed of three representative synthetic brake pads and an AMC brake disc. By integrating interfacial morphology characterization with dynamic modeling, a material–interface–system analytical framework for vibration and noise analysis was established, which revealed the mechanism by which material properties govern the vibration and noise behavior of lightweight friction pairs. The main conclusions are as follows:

(1) The three synthetic brake pads exhibited distinct friction-induced vibration and noise behaviors due to their differences in material composition and mechanical properties. Pad A was found to be rich in graphite and exhibited low hardness, resulting in the lowest friction coefficient and vibration noise amplitude. Pad B has a moderate amount of lubricating phase but the highest surface hardness, resulting in a high and strongly fluctuating friction coefficient, accompanied by significant vibration and noise. Pad C contained the least lubricating phase, but its low material hardness led to a moderate friction coefficient and relatively weak vibration noise.

(2) The variations in interfacial lubrication behavior, wear debris evolution mechanisms, and contact morphology characteristics among the synthetic brake pads significantly affected both the magnitude and time-varying stability of the friction coefficient and contact stiffness. Pad A formed a stable lubricating film at the interface, resulting in a low friction coefficient, while its moderate surface roughness and low hardness contributed to a relatively low normal contact stiffness. Pad C developed the relatively stable third-body layers in localized regions, providing interfacial lubrication and buffering against load fluctuations, which produced a moderate and stable friction coefficient; however, its rough surface and high plastic deformability resulted in the lowest interfacial normal stiffness. Pad B experienced intense shear wear and abrasive plowing with the brake disc, causing a high and sharply

Just Accepted

fluctuating friction coefficient. Nevertheless, its high hardness helped maintain relatively high surface flatness, significantly increasing the interfacial normal stiffness.

(3) The differences in interface friction coefficients and normal contact stiffness among the synthetic brake pads are the fundamental factors driving the variation in vibration and noise responses of lightweight friction pairs. The combined effect of the friction coefficient and contact stiffness governs system stability. When these parameters fall within certain critical ranges, the system is susceptible to modal coupling and instability, leading to pronounced vibration and noise. Among the three synthetic brake pads investigated in this study, only Pad B, which exhibited both a relatively high friction coefficient and a high normal contact stiffness, entered the unstable region and underwent modal coupling, thereby generating vibration and noise levels markedly higher than those of the other two synthetic brake pads.

Acknowledgements

This research was supported by the National Key Research and Development Program of China under Grant No. 2023YFB3710604, the National Natural Science Foundation of China under Grant No. 52388102 and No. U22A20181, the Independent Research Project of the State Key Laboratory of Rail Transit Vehicle System under Grant No. 2024RVL-T09, and the Fundamental Research Funds for the Central Universities under Grant No. 2682024CG008.

Declaration of competing interest

The authors have no competing interests to declare that are relevant to the content of this article.

References

[1] Geng L S. Research and countermeasures on high-quality urban region(suburban) railway development in metropolitan areas. *Modern Urban Transit* (6): 6-11 (2022)

[2] Chen X M, Lurkin V, Wang D, et al. Integrated physical and service network design of suburban

Just Accepted

rail under the coordination of urban rail. *Transportmetrica A: Transport Science* 264: 2302477 (2024)

[3] Li T S, Fan J, Chen X H, et al. Research on the development strategies for operating suburban trains on existing railways. *Railway Standard Design* 70(6): 1-9 (2025)

[4] Li H Q. Discussion on the related problems of through operation of regional rapid rail transit and urban rail transit. *Journal of Railway Engineering Society* 40(2): 89-93 (2023)

[5] Huang X R. Discussion on the optimization path of urban commuting under the guidance of territorial spatial planning: Based on the commuting monitoring report of major cities in China. *Urbanism and Architecture* 21(10): 103-106 (2024)

[6] Zhang C, Shi X, Zhang L. A brief analysis of urban region train type selection and applicable scenarios. *Modern Urban Transit* (2): 27-34 (2024)

[7] González-Gil A, Palacin R, Batty P, et al. A systems approach to reduce urban rail energy consumption. *Energy Conv Manag* 80: 509-524 (2014)

[8] Rochard B P, Schmid F. Benefits of lower mass trains for high speed rail operations. *Proce Inst Civil Eng-Trans* 158(3): 179-182 (2005)

[9] Li D N, Chen L, Mi R H, et al. A review of braking performance and dynamic performance of brake discs. *J Tribol* 147(12): 120801 (2025)

[10] Ware D K, Gay M. Hollow axle developments by london regional transport and british steel. *Proc Inst Mech Eng* 199(D4): 265-274 (1985)

[11] Cao J H, Liang H, Xue J, et al. Research on brake disc lightweight technology based on improving train running quality. *Modern Urban Transit* (11): 47-53 (2019)

[12] Fu K X, Tan D, Qi Y F, et al. Application and challenges of metal matrix composite in rail transit equipment. *Rail transit materials* 2(5): 34-38 (2023)

[13] Mistry P J, Johnson M S. Lightweighting of railway axles for the reduction of unsprung mass and track access charges. *Proc Inst Mech Eng* 234(9): 958-968 (2019)

[14] Chen M L. Research on vehicle selection and train formation for urban region (suburban) railways. *Modern Urban Transit* (6): 6-12 (2024)

[15] Sheng H, Wang Z H, Shao J, et al. Research status and prospect of brake dise materials for high-speed train. *Materials for Mechanical Engineering* 40(1): 1-5 (2016)

[16] Liu J, Dong S, Wang D, et al. Research status of several issues in the design of brake dises for high-speed trains. *Materials Review* 37(14): 69-74 (2023)

[17] Yang Z, Wang Z, Ye S, et al. Braking noise characteristics and a simulation analysis method based on a multiscale braking test. *Journal of Tsinghua University(Science & Technolgy)* 63(10): 1626-
Just Accepted

1639 (2023)

[18] Tran M T, Ang K K. Multiple-railcar high-speed train subject to braking. *Int J Struct Stab Dyn* 17(7): 1750071 (2017)

[19] Wang Q, Wang Z W, Mo J L, et al. A novel dynamics model of a trailer bogie brake system and its application in stability analysis. *Mech Syst Signal Proc* 172: 108966 (2022)

[20] Daoud A, Abou El-Khair M T. Wear and friction behavior of sand cast brake rotor made of A359-20vol% SiC particle composites sliding against automobile friction material. *Tribol Int* 43(3): 544-553 (2010)

[21] Ilanko A K, Vijayaraghavan S. Wear behavior of asbestos-free eco-friendly composites for automobile brake materials. *Friction* 4(2): 144-152 (2016)

[22] Awe S A, Lattanzi L. Comparative evaluation of the tribological performance of al-mmc and gci brake rotors through ak master dynamometer testing. *Lubricants* 13(9): 380 (2025)

[23] Tan D, Xia S H, Yob A, et al. Evaluation of the wear resistance of aluminium-based hybrid composite brake discs under relevant city rail environments. *Mater Des* 215: 110504 (2022)

[24] Baig M M A, Al-Qutub A M, Allam I M, et al. Tribological Performance of Sub-Micron Al2O3-Reinforced Aluminum Composite Brake Rotor Material. *Arab J Sci Eng* 46(3): 2691-2700 (2021)

[25] Pole M, Mukhopadhyay S, Kastamo S, et al. Tribological behavior of hybrid Aluminum-TiB2 metal matrix composites for brake rotor applications. *Wear* 562-563(2025)

[26] Nong X D, Jiang Y L, Fang M, et al. Numerical analysis of novel SiC3D/Al alloy co-continuous composites ventilated brake disc. *Int J Heat Mass Transf* 108: 1374-1382 (2017)

[27] Song P, Yang Z, Xue M, et al. Structural Design of SiCp/A356 Brake Discs Based on Multi-field Coupling and Material Characteristics. *Appl Compos Mater* 31(5): 1515-1546 (2024)

[28] Cao Y L, Zang C X, Wang Z W, et al. Research and optimization of brake noise for lightweight friction pairs in subway vehicles. *Tribology* (2025)

[29] Yang Z, Ye S, Wang Z, et al. Experimental and simulation study on braking noise characteristics and noise reduction strategies of the friction pair between the SiCp/A356 brake disc and the synthetic pad. *Eng Fail Anal* 145(1): 107017 (2023)

[30] Chen F, Ouyang H, Wang X. A new mechanism for friction-induced vibration and noise. *Friction* 11(2): 302-315 (2023)

[31] Ghazaly N M, Ahmed I, El-Sharkawy M. A review of automotive brake squeal mechanisms. *J Mech Des Vib* 1(1): 5-9 (2014)

[32] Wei L, Choy Y S, Cheung C S. The effect of braking conditions on the particular matter emissions and brake squeal. *Wear* 530-531: 205045 (2023)

Just Accepted

[33] Shin M W, Kim Y H, Jang H. Effect of the Abrasive Size on the Friction Effectiveness and Instability of Brake Friction Materials: A Case Study with Zircon. *Tribol Lett* 55(3): 371-379 (2014)

[34] Lazim A R M, Kchaou M, Hamid M K A, et al. Squealing characteristics of worn brake pads due to silica sand embedment into their friction layers. *Wear* 358-359: 123-136 (2016)

[35] Hetzler H, Willner K. On the influence of contact tribology on brake squeal. *Tribol Int* 46(1): 237-246 (2012)

[36] Xiang Z, Mo J, Ouyang H, et al. Contact behaviour and vibrational response of a high-speed train brake friction block. *Tribol Int* 152(2020)

[37] Chen G X, Lv J Z, Zhu Q, et al. Effect of the braking pressure variation on disc brake squeal of a railway vehicle: Test measurement and finite element analysis. *Wear* 426(PartB): 1788-1796 (2019)

[38] Zhu Q, Xie J, Zhang W, et al. Effect of the braking parameter on disc brake squeal of a railway vehicle. *Wear* 522(1): 204884 (2023)

[39] Zhang Q X, Mo J L, Xiang Z Y, et al. Effect of surface micro-grooved textures in suppressing stick-slip vibration in high-speed train brake systems. *Tribol Int* 189(2023)

[40] Liu M, Wang Z, Mo J, et al. Evolution of interface states and stick-slip mechanism of lightweight friction pairs with varying braking pressures. *Wear* 580-581(2025)

[41] Hoffmann N, Fischer M, Allgaier R, et al. A minimal model for studying properties of the mode-coupling type instability in friction induced oscillations. *Mech Res Commun* 29(4): 197-205 (2002)

[42] Zhang Q, Mo J L, Lu X D, et al. Grooved-structure design for improved component damping ability. *Tribol Int* 123: 50-60 (2018)

[43] Miranda G, Buciumeanu M, Costa M M, et al. Metallic reinforcements role on aluminum silicon composites wear behavior. *J Compos Mater* 51(19): 2805-2812 (2017)

[44] Cho M H, Ju J, Kim S J, et al. Tribological properties of solid lubricants (graphite, Sb2S3, MoS2) for automotive brake friction materials. *Wear* 260(7-8): 855-860 (2006)

[45] Gultekin D, Uysal M, Aslan S, et al. The effects of applied load on the coefficient of friction in Cu-MMC brake pad/Al-SiCp MMC brake disc system. *Wear* 270(1-2): 73-82 (2010)

[46] Wang J N, Zafar M Q, Chen Y B, et al. Tribological properties of brake disc material for a high-speed train and the evolution of debris. *Lubricants* 10(8): 168 (2022)

[47] Zhang C, Nadimi S, Maramizonouz S, et al. A discrete element model of high-pressure torsion test to assess the effect of particle characteristics in the interface. *J Tribol-T ASME* 146(8): 081501 (2024)

Just Accepted

[48] Ghosh A, Wang W Y, Sadeghi F. An elastic–plastic investigation of third body effects on fretting contact in partial slip. *Int J Solids Struct* 81: 95-109 (2016)

[49] Lee S, Jang H. Effect of plateau distribution on friction instability of brake friction materials. *Wear* (400): 1-9 (2018)

[50] Fu C J, Zhong M, Xu W H, et al. Synergistic effects of different graphite on the braking performance of Cu-matrix friction materials for high-speed trains based on pin-disc tests. *Tribol Trans* 65(6): 1008-1021 (2022)

[51] Davide T, Francesco M, Mario S, et al. Estimation of the normal contact stiffness for frictional interface in sticking and sliding conditions. *Lubricants* 7(7): 56 (2019)

[52] Mandelbrot B B. Stochastic models for the Earth's relief, the shape and the fractal dimension of the coastlines, and the number-area rule for islands. *Proceedings of the National Academy of Sciences* 72(10): 3825-3828 (1975)

[53] Mu X K, Sun W, Liu C, et al. Numerical Simulation and Accuracy Verification of Surface Morphology of Metal Materials Based on Fractal Theory. *Materials* 13(18): 4158 (2020)

[54] Berry M V, Lewis Z V. On the Weierstrass-Mandelbrot fractal function. *Proceedings of the Royal Society of London A Mathematical and Physical Sciences* 370(1743): 459-484 (1997)

[55] Zhu C X, Yan Z B. Research on the micro and dynamic characteristics of combination surface based on fractal theory. *Mech Sci* 11(1): 1-27 (2020)

[56] Wang C H, Li S J, Li Y, et al. Prediction of formation abrasiveness under the action of a PDC bit based on the fractal dimension of a rock surface. *Sci Rep* 14(1): 1-13 (2024)

[57] Yan W, Komvopoulos K. Contact analysis of elastic-plastic fractal surfaces. *J Appl Phys* 84(7): 3617-3624 (1998)

[58] Komvopoulos K, Yan W. A fractal analysis of stiction in microelectromechanical systems. *J Tribol* 119(3): 391-400 (1997)

[59] Bhushan B, Majumdar A. Elastic-plastic contact model for bifractal surfaces. *Wear* 153(1): 53-64 (1992)

[60] Zhang Q X, Liu Q-A, Mo J L, et al. Analysis of contact characteristics and dynamic response of joint interface with surface micro-grooved texture based on fractal theory. *Mech Syst Signal Proc* 218: 111553 (2024)

[61] Wang Q, Wang Z, Mo J. A hybrid friction-induced vibration form: Experimental measurement and mechanism discussion. *Tribol Int* 183(1): 108397 (2023)

Author biography

Just Accepted

Caiqi Liao received her M.S. degree in instrument science and technology from Jiangsu University in 2022, China. Now, she is a Ph.D. student at the School of Mechanical Engineering, Southwest Jiaotong University, China. Her research interests include vibration and noise and tribo-dynamics.

Qixiang Zhang received his Ph.D. degree in mechanical design and theory from Southwest Jiaotong University, China, in 2025. He is currently a postdoctoral researcher at Southwest Jiaotong University, China. His research interests include friction, vibration and noise control and fault diagnosis and identification for high-speed train braking systems.

Just Accepted